

# SCIENTIFIC REPORTS



OPEN

## Magnetic domain interactions of Fe<sub>3</sub>O<sub>4</sub> nanoparticles embedded in a SiO<sub>2</sub> matrix

J. A. Fuentes-García<sup>1</sup>, A. I. Diaz-Cano<sup>1</sup>, A. Guillen-Cervantes<sup>2</sup> & J. Santoyo-Salazar<sup>2</sup>

Currently, superparamagnetic functionalized systems of magnetite (Fe<sub>3</sub>O<sub>4</sub>) nanoparticles (NPs) are promising options for applications in hyperthermia therapy, drug delivery and diagnosis. Fe<sub>3</sub>O<sub>4</sub> NPs below 20 nm have stable single domains (SSD), which can be oriented by magnetic field application. Dispersion of Fe<sub>3</sub>O<sub>4</sub> NPs in silicon dioxide (SiO<sub>2</sub>) matrix allows local SSD response with uniaxial anisotropy and orientation to easy axis, 90° <001> or 180° <111>. A successful, easy methodology to produce Fe<sub>3</sub>O<sub>4</sub> NPs (6–17 nm) has been used with the Stöber modification. NPs were embedded in amorphous and biocompatible SiO<sub>2</sub> matrix by mechanical stirring in citrate and tetraethyl orthosilicate (TEOS). Fe<sub>3</sub>O<sub>4</sub> NPs dispersion was sampled in the range of 2–12 h to observe the SiO<sub>2</sub> matrix formation as time function. TEM characterization identified optimal conditions at 4 h stirring for separation of SSD Fe<sub>3</sub>O<sub>4</sub> in SiO<sub>2</sub> matrix. Low magnetization (M<sub>s</sub>) of 0.001 emu and a coercivity (H<sub>c</sub>) of 24.75 Oe indicate that the embedded SSD Fe<sub>3</sub>O<sub>4</sub> in amorphous SiO<sub>2</sub> reduces the M<sub>s</sub> by a diamagnetic barrier. Magnetic force microscopy (MFM) showed SSD Fe<sub>3</sub>O<sub>4</sub> of 1.2 nm on average embedded in SiO<sub>2</sub> matrix with uniaxial anisotropy response according to Fe<sup>3+</sup> and Fe<sup>2+</sup> electron spin coupling and rotation by intrinsic Néel contribution.

The addressable Fe<sub>3</sub>O<sub>4</sub> NPs in functionalized systems are of interest for the development of applications in magnetic hyperthermia, drug delivery and diagnosis agents and alternative cancer treatments due to their high biocompatibility<sup>1–3</sup>, bioactivity<sup>4,5</sup>, driving accumulation<sup>6,7</sup> and magnetic excitation<sup>8–10</sup> features. The systems based on superparamagnetic NPs behaviour have either biological or technological potential applications. Fe<sub>3</sub>O<sub>4</sub> NPs have been extensively studied due to their interesting properties, which allow their evaluation and potential application as catalytic agents<sup>11–13</sup>, gas sensors<sup>14</sup>, water treatment agents<sup>15</sup>, environmental remediation agents<sup>16–18</sup> magnetic resonance contrast agents<sup>1,19</sup>, ferrofluids<sup>20</sup>, data storage devices<sup>21</sup>, and electronic devices<sup>22</sup>. Superparamagnetic Fe<sub>3</sub>O<sub>4</sub> NPs with SSD have crystal anisotropy in the order 1.1, which allows easy reorientation and energy exchange to generate magnetic hyperthermia in presence of a magnetic field AC<sup>23</sup>. However, avoiding Fe<sub>3</sub>O<sub>4</sub> NPs agglomeration due to interactions between neighbours is a challenge for biological applications. One alternative is separating the Fe<sub>3</sub>O<sub>4</sub> SSD considerable distances by embedding them in a negatively charged, amorphous SiO<sub>2</sub> matrix<sup>24</sup>. This method allows a local response orientation of SSD to be obtained, according to Majetich S. A. *et al.*; if neighbouring superparamagnetic particles with a low anisotropy are coupled by exchange or dipolar interactions, their optimal separation for the maximum coercivity will allow the configuration of individually addressable SSD<sup>25</sup>. The local interactions will be the same, if the Fe<sub>3</sub>O<sub>4</sub> particle size is similar. Then, SSD will have coherent rotation and contribute to the effective energy exchange by hyperthermia.

Current implementation of these systems depends on the superparamagnetic particle size (<20 nm) and SSD anisotropy, which directly influence the stability, dissipated energy and magnetic properties as function of time, such as the magnetic susceptibility and coercive field<sup>26</sup>. For this reason, different investigations have developed different methods to stabilize Fe<sub>3</sub>O<sub>4</sub> NPs while preserving the main SSD properties<sup>27–29</sup>. V Reichel *et al.* showed that the magnetic properties of magnetite are dependent on Néel relaxation. These depend on the particle size, morphology and interparticle interactions as well as the temperature and time-scale of the measurement in Fe<sub>3</sub>O<sub>4</sub> NPs (9 ± 3 nm)<sup>30</sup>. The SiO<sub>2</sub> media can be used to give Fe<sub>3</sub>O<sub>4</sub> NPs specific accumulation in organs or tissues

<sup>1</sup>UPIITA-Instituto Politécnico Nacional, 07340, Ciudad de México, Mexico. <sup>2</sup>Departamento de Física, Centro de Investigación y de Estudios Avanzados del Instituto Politécnico Nacional, CINVESTAV-IPN, Av. IPN 2508, Zacatenco, 07360, Ciudad de México, Mexico. Correspondence and requests for materials should be addressed to J.S.-S. (email: [jsantoyo@fis.cinvestav.mx](mailto:jsantoyo@fis.cinvestav.mx))

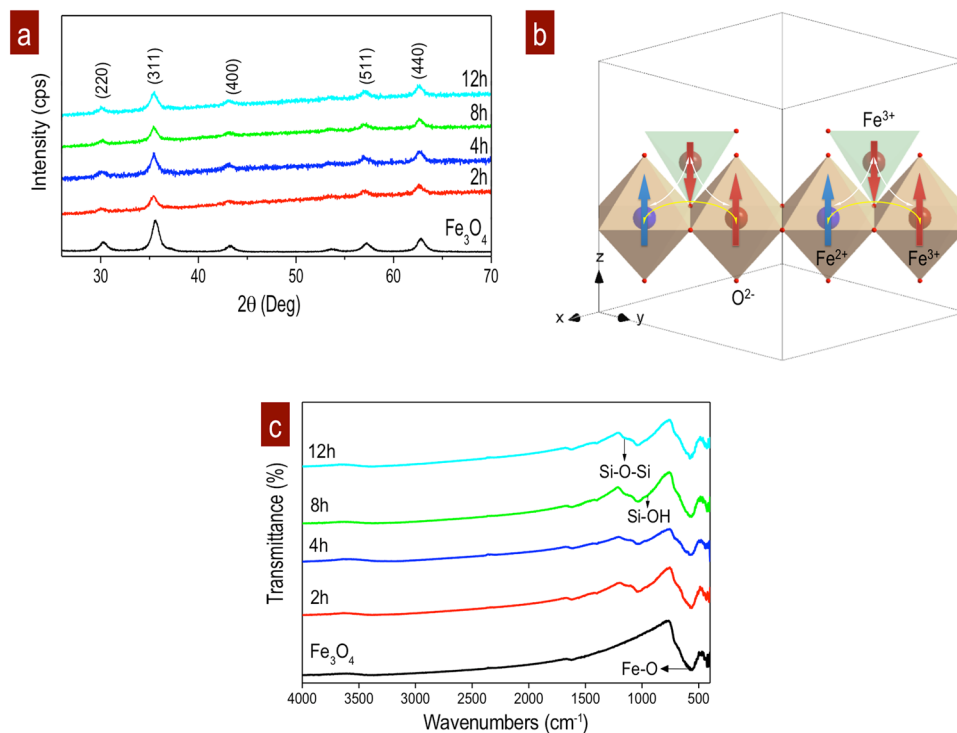


**Figure 1.** Structure and bonds of  $\text{Fe}_3\text{O}_4$  NPs embedded in  $\text{SiO}_2$  matrix. (a) XRD shows the evolution with the stirring time;  $\text{Fe}_3\text{O}_4$  NPs reference;  $\text{Fe}_3\text{O}_4$  NPs+ $\text{SiO}_2$  matrix at 2, 4, 8, and 12 h. Background at these time is associated with the amorphous  $\text{SiO}_2$  matrix and small displacement of peaks due to  $\text{Fe}_3\text{O}_4$  surface oxidation. (b) Ferromagnetic structure with octahedral sites of  $\text{Fe}^{2+}$  and  $\text{Fe}^{3+}$  contributes to the magnetic alignment of  $\text{Fe}_3\text{O}_4$  NPs under magnetization. (c) FT-IR spectra of uncoated  $\text{Fe}_3\text{O}_4$  NPs and those in the  $\text{SiO}_2$  matrix at 2, 4, 8 and 12 h of the coating reaction.

through bio-functionalization<sup>31–35</sup> because it is an interaction-capable surface with ligands related to biological molecules.

Successful stabilization of  $\text{Fe}_3\text{O}_4$  NPs with  $\text{SiO}_2$  can be achieved by using citrate as a dispersing agent. The polymerization time of  $\text{SiO}_2$  was considered in the range of 2–12 h. However,  $\text{Fe}_3\text{O}_4$  functionalization and interaction media barriers with organic products can reduce  $M_s$ . The magnetic response will depend on the volume, particle form and SSD population density in the system<sup>36</sup>. Rotation SSD  $\text{Fe}_3\text{O}_4$  will depend on the intrinsic structure defined Néel interactions and magnetic moment distribution per volume unit by the easy axis crystal orientation,  $\langle 100 \rangle$  or  $\langle 111 \rangle$  and the coercivity terms, which are crucial for SSD uniaxial response<sup>37</sup>. The routes to control the dispersion  $\text{Fe}_3\text{O}_4$  NPs embedded in  $\text{SiO}_2$  help to consolidate well defined the local SSD and their magnetic interactions. Superparamagnetic  $\text{Fe}_3\text{O}_4$  NPs dispersions in an inorganic matrix allow the creation of a functional target or hyperthermia generators with potential applications in nanomedicine<sup>38,39</sup>.

## Results and Discussion

The key to obtaining  $\text{Fe}_3\text{O}_4$  NPs is the ion relation  $\frac{1}{2} \text{Fe}^{2+} : \text{Fe}^{3+}$  by co-precipitation and the additional dispersion reaction by Stöber route. These ions were dispersed with citrate and TEOS to produce  $\text{Fe}_3\text{O}_4$  in an amorphous  $\text{SiO}_2$  matrix according to the methodology described by L. Yang *et al.*<sup>40</sup> with some modifications.

XRD results show the main crystalline reflections of  $\text{Fe}_3\text{O}_4$  NPs with a cubic inverse spinel structure, forming a close packing *fcc* ( $a = 8.396 \text{ \AA}$ )<sup>41</sup>, Fig. 1a. Ferromagnetic spin interactions are defined by divalent  $\text{Fe}^{2+}$  and trivalent  $\text{Fe}^{3+}$  occupying octahedral sites and a double-exchange mechanism, while  $\text{Fe}^{3+}$  tetrahedral sites form an antiferromagnetic response, Fig. 1b. Because of superexchange, oxygen-mediated coupling, all the magnetic moments of the tetrahedral iron ions are aligned in a specific direction, while all the octahedral iron magnetic moments are aligned in the opposite direction<sup>42</sup>.

The spectra (Fig. 1a (2–12 h)) show the amorphous contribution of the  $\text{SiO}_2$  matrix and the  $\text{Fe}_3\text{O}_4$  NPs, which do not lose their crystalline quality. Wide diffraction peaks from the  $\text{Fe}_3\text{O}_4$  NPs are observed in an amorphous curve for the entire stirring range of 2–12 h. The fluorescence increased and the intensities decreased for each reflection in the patterns corresponding to the  $\text{Fe}_3\text{O}_4$  NPs embedded in the  $\text{SiO}_2$  matrix. This is attributed to the confinement of the  $\text{Fe}_3\text{O}_4$  NPs inside the amorphous  $\text{SiO}_2$  matrix.

Additionally, wide peaks are related to the nanometric particle size. Some changes in the NPs size were observed as a function of the reaction time, Fig. 1a. Supplementary information (s1) shows the FWHM values and sizes obtained through a modified Scherrer analysis by using a pseudo-Voigt function<sup>43</sup>. In some cases, the size of the particle increased due to agglomeration and the dynamic stirring energy. When the  $\text{SiO}_2$  matrix does not complete the polymerization, the uncoated  $\text{Fe}_3\text{O}_4$  NPs form aggregates and reassemble<sup>30</sup>. Peaks of smaller

particle sizes were defined after the stabilized reaction of the NPs in the SiO<sub>2</sub> matrix with 4 h of processing. Average size in Fe<sub>3</sub>O<sub>4</sub> NPs was 16.73 nm and  $a = 8.394 \text{ \AA}$ . Average sizes and lattice parameters in Fe<sub>3</sub>O<sub>4</sub> NPs+SiO<sub>2</sub> matrix were (a) 16.49 nm and 8.360 Å at 2 h, (b) 15.37 nm and 8.3641 Å at 4 h, (c) 16.92 nm and 8.3619 Å at 8 h, and (d) 17.07 nm and 8.3614 Å. The lattice parameters showed small distortions as Fe<sub>3</sub>O<sub>4</sub>@ $\gamma$ -Fe<sub>2</sub>O<sub>3</sub> by surface NPs oxidation.

The FT-IR spectra of different samples are presented in Fig. 1c. The interactions of the functional group Fe<sub>3</sub>O<sub>4</sub> NPs in the SiO<sub>2</sub> matrix can be observed. Characteristic iron-oxygen bond (Fe-O) signals at approximately 585 cm<sup>-1</sup> are in the five spectra. Crystalline Fe<sub>3</sub>O<sub>4</sub> is conserved after the embedding process. Also, it is possible to identify the SiO<sub>2</sub> contributions in Fig. 1c; a broad band centred at 1048 cm<sup>-1</sup> is observed. There are also two interactions of interest at 1113 cm<sup>-1</sup>, which is attributed to the Si-O-Si bonds, and another at 986 cm<sup>-1</sup>, which is due to the Si-OH groups from the matrix. These interactions slightly increased in intensity with the reaction time, which promoted the SiO<sub>2</sub> layer thickness. No additional linkage interactions were observed for the functional groups characteristic of citrate and the stabilizing agents used during the experiment. These were completely removed during the particle washing step. This indicates that the reaction parameters, such as the concentration of the solutions and the reaction times, allow the dispersed particles to be obtained without adsorbed citrate molecules on the surface of the Fe<sub>3</sub>O<sub>4</sub> NPs.

TEM results for Fe<sub>3</sub>O<sub>4</sub> NPs embedded in SiO<sub>2</sub> matrix as a function of time are shown in Fig. 2. The evolution of the processing was observed at 2, 4, 8 and 12 h of stirring: (1) Agglomeration of Fe<sub>3</sub>O<sub>4</sub> NPs at 2 h, Fig. 2(a-c). Selected area of electron diffraction (SAED) results correspond to Fe<sub>3</sub>O<sub>4</sub> structure with a low amorphous contribution from SiO<sub>2</sub>. (2) Good dispersion of individual Fe<sub>3</sub>O<sub>4</sub> NPs at 4 h, Fig. 2(d-f). Under these conditions, the small, agglomerated nanoparticle entities are dispersed, and the TEOS polymerization is consolidated. SiO<sub>2</sub> contributes a negative charge between the NPs to form individual SSD, Fig. 2f. SAED shows the contribution of Fe<sub>3</sub>O<sub>4</sub> NPs and the amorphous matrix of SiO<sub>2</sub>. The crystalline Fe<sub>3</sub>O<sub>4</sub> structure diffracted in the planes (220), (311) and (440). (3) The regions of agglomerated Fe<sub>3</sub>O<sub>4</sub> NPs plus SSD dispersed for 8 h of stirring, Fig. 2(g-i). Under these conditions, there are NPs linked by electrostatic interactions and/or dipolar coupling. SAED shows the crystalline contribution of Fe<sub>3</sub>O<sub>4</sub> NPs with diffraction planes in (311) and (440)<sup>44</sup>. The agglomerates increased in size. (4) Agglomerates plus isolated SSD were obtained in the SiO<sub>2</sub> matrix after 12 h of stirring, Fig. 2(j-l). This phenomenon is associated with the strong interaction between neighbours. SAED shows the rings of the diffraction planes of Fe<sub>3</sub>O<sub>4</sub>, which are very similar in intensity to those in Fig. 2c. It could be said that the matrix of SiO<sub>2</sub> formed at 4 h stirring is a negatively charged film that confines the SSD as individual entities. As the agitation time is increased to 8–12 h, the dynamic movement increases the coalitions between NPs and their interactions. As consequence, the attraction between NPs increases the agglomeration with a long agitation time.

The main challenge in potential applications of Fe<sub>3</sub>O<sub>4</sub> NPs lies in their superparamagnetic properties, uniaxial anisotropy, particle size and form. Typically, bulk Fe<sub>3</sub>O<sub>4</sub> has a  $M_s$  of 91 emu/g, and its inner structure forms multidomains with magnetic anisotropic axial ratios larger than 5<sup>45,46</sup>. In superparamagnetic NPs, the magnetic anisotropic energy barrier is reduced and allows the rotation of SSD from a spin-up state to spin-down state to readily rotate the magnetic spin direction on the easy axis<sup>47</sup>. The magnetization from Fe<sub>3</sub>O<sub>4</sub> NPs embedded in a SiO<sub>2</sub> matrix shows superparamagnetic, closed hysteresis loops<sup>48</sup>. As the particle size of Fe<sub>3</sub>O<sub>4</sub> decreased below the superparamagnetic diameter,  $M_s$  decreases as well, and the magnetic fluctuation leads to a small  $H_c$  near zero with a low remanence at 300 K<sup>49</sup>. Samples as a function of the stirring time were  $M_s = 0.0015 \text{ emu}$ ,  $H_c = 26.480 \text{ Oe}$  at 2 h;  $M_s = 0.0010 \text{ emu}$ ,  $H_c = 24.000 \text{ Oe}$  at 4 h;  $M_s = 0.0013 \text{ emu}$ ,  $H_c = 24.800 \text{ Oe}$  at 8 h; and  $M_s = 0.0015 \text{ emu}$ ,  $H_c = 25.570 \text{ Oe}$  at 12 h, Fig. 3a. Additionally, the TEM image showed the separation of the Fe<sub>3</sub>O<sub>4</sub> NPs SSD embedded in the SiO<sub>2</sub> matrix at 4 h of stirring. These parameters and the particle size are directly related to the descending  $H_c$  value as follows: (a) agglomerations of NPs 11.70 nm on average at 2 h; (b) fragmentation and dispersion of 5.64 nm NPs with distances from 5.54 to 29.21 nm as individual SSD in SiO<sub>2</sub> at 4 h; (c) aggregates of 15.45 nm NPs on average and individual 4.47 nm NPs on average separated by 3.54 nm to 6.00 nm in SiO<sub>2</sub> at 8 h; and (d) 13.7 nm average agglomerates and 6.02 nm NPs on average separated by distances 5.20 nm to 6.43 nm in SiO<sub>2</sub> at 12 h. Coherent results were obtained by  $M_s$  and  $H_c$  with 4 h of stirring. This means that individual SSD have uniaxial anisotropy and are addressable by the separation between the NPs, Fig. 3c. However, in case of the polydispersion of NPs,  $M_s$  and  $H_c$  increase due to the major volume contribution from the neighbouring interactions and thermal fluctuations. The diamagnetic SiO<sub>2</sub> barrier around the Fe<sub>3</sub>O<sub>4</sub> NPs reduces  $M_s$ . However, separation between the monodispersed NPs maintains the  $H_c$  as local SSD. These effects can also be observed in encapsulated Fe<sub>3</sub>O<sub>4</sub> NPs with organic chains. Some organic coating media have important roles due their permeability, specificity and individual drive of the magnetic domains that can be accumulated in tumours<sup>50</sup>. The integration of SSD as functionalized systems at optimal distances and relatively high  $H_c$  values would increase the hyperthermia efficiency by magnetic field AC excitation in the frequency range 100 kHz–500 MHz<sup>51</sup>.

Fe<sub>3</sub>O<sub>4</sub> NPs distribution embedded in the SiO<sub>2</sub> matrix were observed by atomic force microscopy. The 3D images show the differences in the dispersed nanoparticles according the stirring time for 4 and 12 h. Figure 4. The sample obtained with 4 h of stirring had local, isolated particles in the SiO<sub>2</sub> matrix, Fig. 4a. The topography profiles show an estimated particle size of 6 nm and roughness of MRS = 4.53 nm. The images with 12 h of stirring showed 21.8 nm agglomerated particles and their neighbouring interactions with an MRS = 3.07 nm, Fig. 4b. The profiles below 3D images are associated to particle size and their agglomerations in both cases.

MFM shows the magnetic moment density per volume unit. The 3D images are generated by the interaction of magnetic tip polarization, which is normal with respect to the NPs surface, and sensing of the attractive and repulsive states<sup>48</sup>. SSD are NPs that can be aligned in parallel by exchanging forces of the electron spins from applied magnetic field. Inner magnetic structure Fe<sub>3</sub>O<sub>4</sub> SSD with Fe<sup>+3</sup> and Fe<sup>+2</sup> electron spin coupling respond uniaxially because magneto-crystalline anisotropy forces tend to align in a preferred direction based on the easy axis. For superparamagnetic sizes, the relative magnitude of the boundary energy becomes larger than the magnetostatic energy. At a critical size, the spin direction can be oriented by exchange interactions in the SSD<sup>37</sup>.

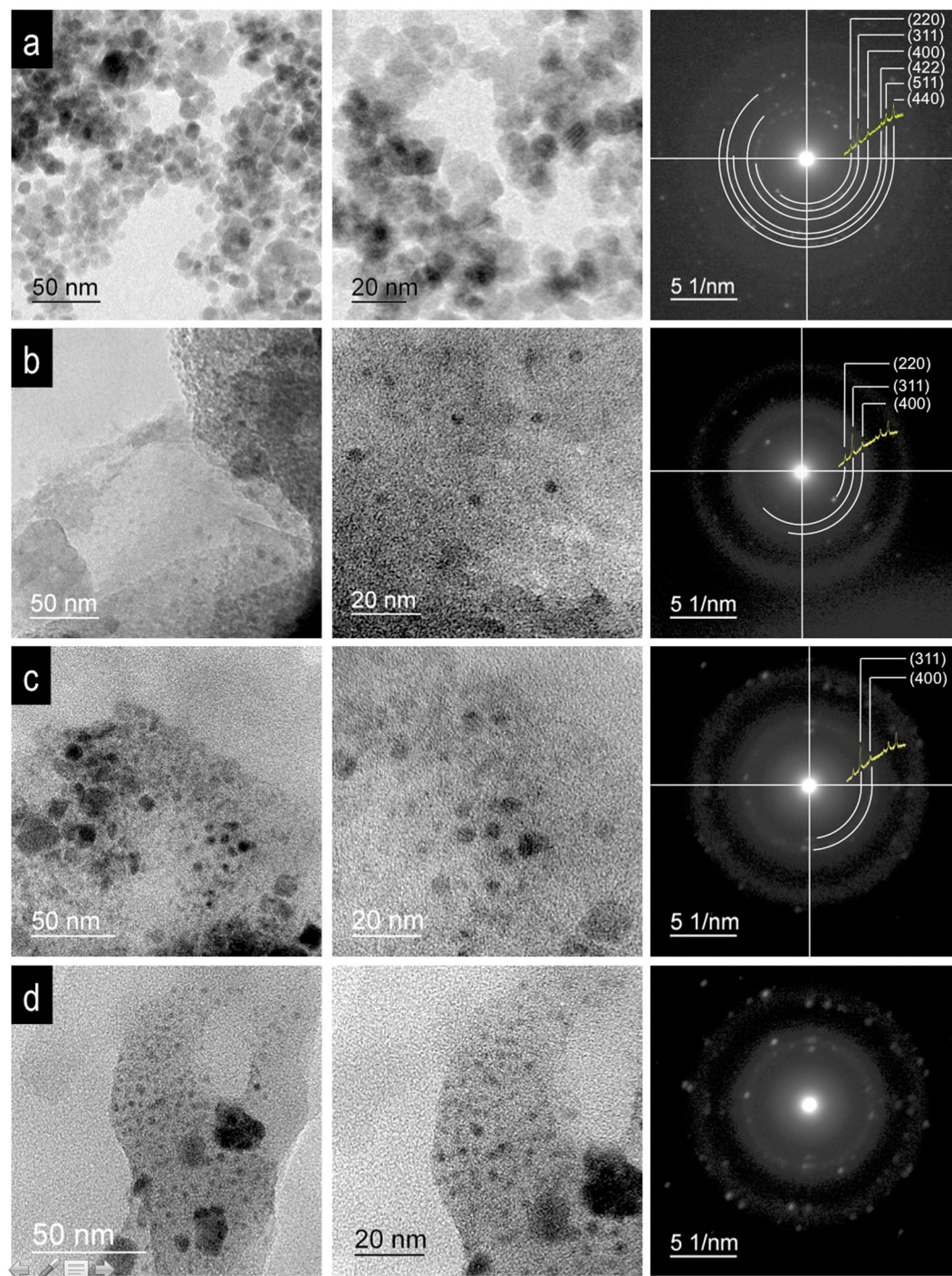


**Figure 2.** TEM images show the dispersion of  $\text{Fe}_3\text{O}_4$  NPs at different reaction times in the  $\text{SiO}_2$  matrix: (a,b) Agglomeration of NPs at 2 h and (c) SAED with characteristic rings of the  $\text{Fe}_3\text{O}_4$  NPs; the intensity depends on the population density of NPs; (d,e) individual SSD in the  $\text{SiO}_2$  matrix after 4 h and (f) SAED with dispersion in amorphous  $\text{SiO}_2$  plus  $\text{Fe}_3\text{O}_4$  NPs; (g,h) SSD+agglomeration of NPs at 8 h, and (i) SAED with dispersion in amorphous  $\text{SiO}_2$ ; agglomeration increases the intensity of the electron diffraction; (j,k) SSD+agglomeration of NPs; (l) diffraction is increased by the groups of NPs agglomerates.

MFM 3D images showed surface of NPs by magnetization  $H \uparrow$  and demagnetization  $H = 0$  effects from  $\text{Fe}_3\text{O}_4$  SSD embedded in the  $\text{SiO}_2$  matrix. The magnetic interaction at the tip in the lift mode shows the disorder from the intrinsic structure at  $H = 0$ . Under the saturation measurement conditions  $H \sim 1200$  Oe for the Co-Ni tip, the SSD uniaxial orientation of the magnet is shown with the domains oriented at  $90^\circ$  for the majority  $n \uparrow$  and minority  $n \downarrow$  states with  $H \uparrow$ <sup>48</sup>. Finally, domain disorder is observed by demagnetization under the initial conditions  $H = 0$ . When the magnetic field AC is applied to these systems, the magnetic domains will fluctuate with local vibrations and will transform this energy into thermal energy. The orientation was observed in a non-continuous media

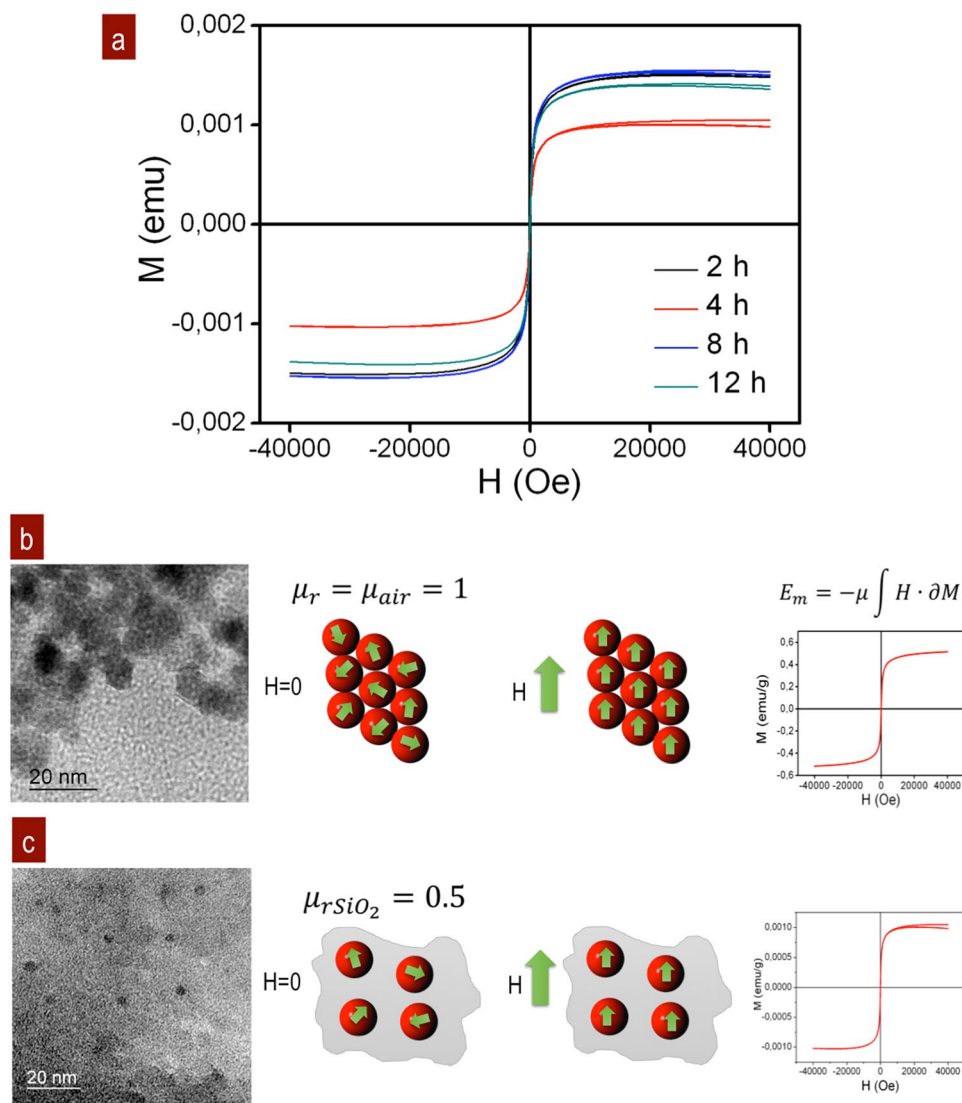


**Figure 3.** Magnetization responses from  $\text{Fe}_3\text{O}_4/\text{SiO}_2$ : (a)  $H$  vs  $M$  as a function of the stirring time for well dispersed NPs as individual SSD at 4 h shows a lower magnetization. The amorphous  $\text{SiO}_2$  barrier between NPs reduces the magnification of 2, 4, 8, and 12 h of processing. Superparamagnetic signals as close loops were observed in all cases. (b,c) Differences in the magnetization due to the changes in the magnetic permeability. The magnetization saturation decreases with the  $\mu_r$  of the  $\text{SiO}_2$  matrix media and the separation of NPs as SSD.

with local SSD interactions at 4 h of stirring, Fig. 5(a–c). In the case of NPs agglomeration, the surface interactions showed a global response by addition of all magnetic domains in the 12 h stirring sample, Fig. 5(d–f).

Zoom was performed under the saturation conditions  $H \uparrow$  to show the uniaxial behaviour. Parallel stripes from attractive and repulsive interactions define the magnetic domains. The exchange forces of the parallel alignment are result of the internal magnetic structure in  $\text{Fe}_3\text{O}_4$  NPs, which are defined by Néel interactions, Fig. 6. The profiles show the  $\theta$  (deg) and domains oriented in the normal direction,  $90^\circ$ , with average domain sizes of 1.2 nm and uniaxial anisotropy from main crystalline direction<sup>37</sup>. The anisotropy energy is given by  $E_a = KV \sin^2 \theta$ , where  $K$  is a typical constant of the material,  $V$  is the volume of the particle,  $\theta$  is the angle between the magnetization and the easy axis. The local response of  $\text{Fe}_3\text{O}_4$  NPs showed magnetic domains with an average size of 1.2 nm surrounded by the  $\text{SiO}_2$  matrix with stirring for 4 h. The profile defines the parallel interactions of the uniaxial response, Fig. 6a–c. However, the neighbouring interactions of  $\text{Fe}_3\text{O}_4$  NPs in  $\text{SiO}_2$  matrix with 12 h of stirring show well-defined interactions in the same direction as the sum of local interactions with similar magnetic domains in the range of 1.2 nm, Fig. 6d,e. The  $\text{Fe}_3\text{O}_4$  SSD in the  $\text{SiO}_2$  matrix show a local response of addressable superparamagnetic behaviour, which is mainly governed by particle size and shape of  $\text{Fe}_3\text{O}_4$  cores in a monodispersion at magnetic field saturation. The degree axis in the profiles shows the deflection propensity in attraction and repulsion generated by  $H \uparrow$ , and these values can change based on the roughness topography and  $H \uparrow$  intensity to form field lines between the tip and sample. The differences in the tip deflections from the SSD were  $-33.1^\circ - (-39.1^\circ) = 6.0^\circ$  at 4 h of stirring, Figs. 6c, and  $-9.4^\circ - (-16.6^\circ) = 7.2^\circ$  at 12 h of stirring, Fig. 6f, which are very

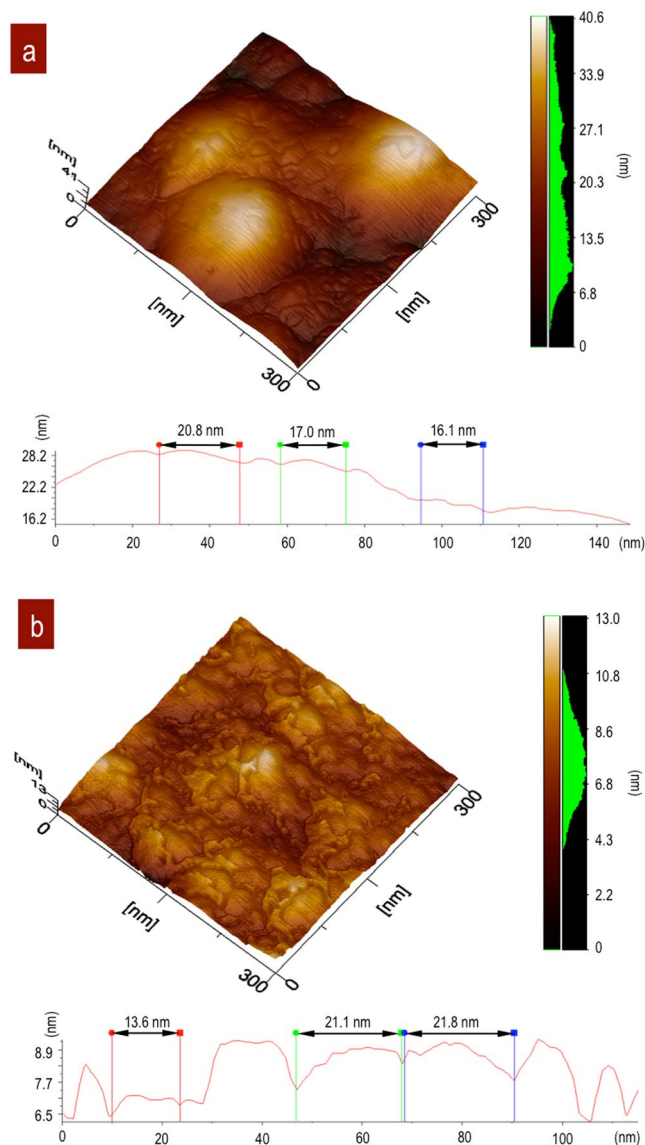


**Figure 4.** Topography by AFM. **(a)**  $\text{Fe}_3\text{O}_4$  NPs immersed in a  $\text{SiO}_2$  matrix after 4 h of stirring. **(b)** 12 h of stirring with a high concentration of NPs. Profiles show isolated  $\text{Fe}_3\text{O}_4$  NPs signals from **(a)** SSD at 4 h and agglomeration at 12 h **(b)**.

similar. These results show the uniaxial responses of local SSD of individual NPs at 4 h and the sum of the SSD as a continuum in the NPs agglomeration at 12 h.

Typically  $H_c$  decreases as a function of particle size in  $\text{Fe}_3\text{O}_4$  NPs with close hysteresis loop. However, the superparamagnetic single-domains response of  $\text{Fe}_3\text{O}_4$  NPs is maintained by local response SSD as agglomeration phenomena is reduced in the case of  $\text{SiO}_2$  matrix due to its permeability<sup>47</sup>. According to Dave S., R. Dave and G. Xiaohu, the formation of the domain walls is a process driven by the balance between the magnetostatic energy as a function of the particle size<sup>52</sup>.

## Conclusions

The synthesis strategy presented is a fast and effective option to avoid the agglomeration phenomenon of  $\text{Fe}_3\text{O}_4$  NPs by stabilizing them in  $\text{SiO}_2$  as a function of the stirring time without altering their crystalline features.

The  $H_c$  is maintained in individual  $\text{Fe}_3\text{O}_4$  SSD with uniaxial behaviour at 4 h of stirring. MFM showed SSD and that local NPs in the  $\text{SiO}_2$  matrix have similar responses as the NPs concentration increases. However,  $M_s$  is reduced by the distance between the NPs among the  $\text{SiO}_2$  matrix, and this depends on the permeability of the media. Néel interactions produce local fluctuations and energy transference from reorientable SSD by magnetic fields at high frequencies. The challenge is to control the  $\text{Fe}_3\text{O}_4$  SSD as individuals in organic media to increase the response velocity and effective magnetic excitation to produce hyperthermia.

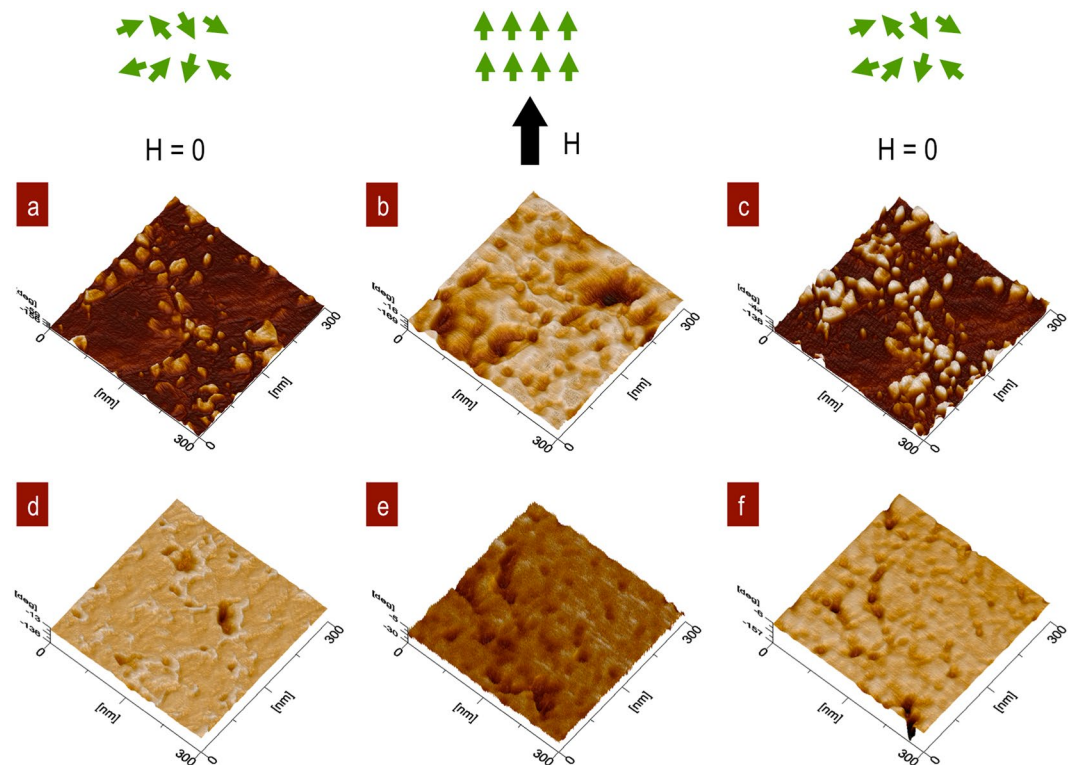


**Figure 5.** Magnetic domain interactions for the magnetization and demagnetization of (a)  $\text{Fe}_3\text{O}_4$  NPs immersed in a  $\text{SiO}_2$  matrix after stirring for 4 h,  $H = 0$ ; (b) orientation of the SSD at  $H = 12000$  Oe; (c) at  $H = 0$ , the sample showed the local SSD orientation under the saturation conditions of the applied field; (d) agglomeration of NPs in a  $\text{SiO}_2$  matrix after 12 h at  $H = 0$ ; (e) orientation of the NPs at  $H = 12000$  Oe; and (f) disorder of the NPs at  $H = 0$ .

$\text{Fe}_3\text{O}_4$  NPs embedded in a  $\text{SiO}_2$  matrix are candidates as functional groups or specific organic linkers for cancer cell interactions and hyperthermia therapy. The development of dispersed SSD is mandatory to improve biological applications.

## Materials and Methods

For the synthesis, hydrochloric acid (HCl) (36.5–38.0%, BAKER ANALYZED ACS), deionized water (Millipore, 18.2 M $\Omega$  cm), iron chloride II ( $\text{FeCl}_2$ , 98%), iron chloride III (97%), a tetramethyl ammonium solution ( $\text{C}_4\text{H}_{13}\text{NO}$ , 25 wt% in  $\text{H}_2\text{O}$ ), tetraethyl orthosilicate (TEOS, 98%), a 28% ammonium hydroxide solution ( $\text{NH}_4\text{OH}$ ) and absolute ethyl alcohol ( $\text{C}_2\text{H}_5\text{OH}$ ) were all from Sigma-Aldrich and used as received without any purification.

**Synthesis of  $\text{Fe}_3\text{O}_4$  NPs.** The formation of nanostructured magnetite through a co-precipitation method<sup>49</sup> was realized via the following: an aqueous solution of hydrochloric acid (HCl, 0.64 N) was prepared to dissolve the precursor salts of the  $\text{Fe}^{+2}$  (ferrous chloride,  $\text{FeCl}_2$ ) and  $\text{Fe}^{+3}$  ions (ferric chloride,  $\text{FeCl}_3$ ).

After the acidic solution was prepared, 6.25 mL was taken, and 2.52 g of  $\text{FeCl}_2$  was added. Another 25 mL of the solution was used to dissolve 6.99 g of  $\text{FeCl}_3$ , and both solutions were kept under magnetic stirring for 1 h. Then, both solutions were mixed in a round-bottom, three-necked flask and bubbled with Ar for 5 min to remove any dissolved oxygen in the solution. The resultant solutions were stirred at 500 rpm and heated to 70 °C. Once the temperature stabilized, 21 mL of tetramethylammonium hydroxide was added dropwise, providing an alkaline environment for the formation of the magnetite. The solution turned black, which was an indication that iron oxide formed in the solution. After 40 min, the stirring and heating were stopped, and the mixture was allowed to cool to room temperature. The nanoparticles were washed with water and precipitated with the aid of a magnet until the pH of the dispersion was equal to 7. Once the nanoparticles were dispersed in water, they were freeze-dried for 12 h to obtain the magnetite powder.

**Synthesis of  $\text{Fe}_3\text{O}_4$  in a  $\text{SiO}_2$  matrix.** The  $\text{Fe}_3\text{O}_4$  NPs powder (0.02 g) was taken and mixed with the same amount of citrate in an aqueous solution (250 mL) and mechanically stirred at 500 rpm for 1 h. Citrate was used as a dispersal agent to avoid agglomeration of the nanostructures prior to the formation of the  $\text{SiO}_2$  matrix.

Then, the  $\text{SiO}_2$  precursor solution was prepared as follows: 10 mL of water, 50 mL of ethanol, 5 mL of ammonium hydroxide and 0.2 mL of TEOS were mixed by magnetic stirring for 10 min. After that, the solution of magnetite and citrate was mixed with the  $\text{SiO}_2$  precursor solution. To modify the thickness of the  $\text{SiO}_2$  coating, the mixture reacted for 2, 4, 8 and 12 h under mechanical stirring at 500 rpm. Once the different times passed, the

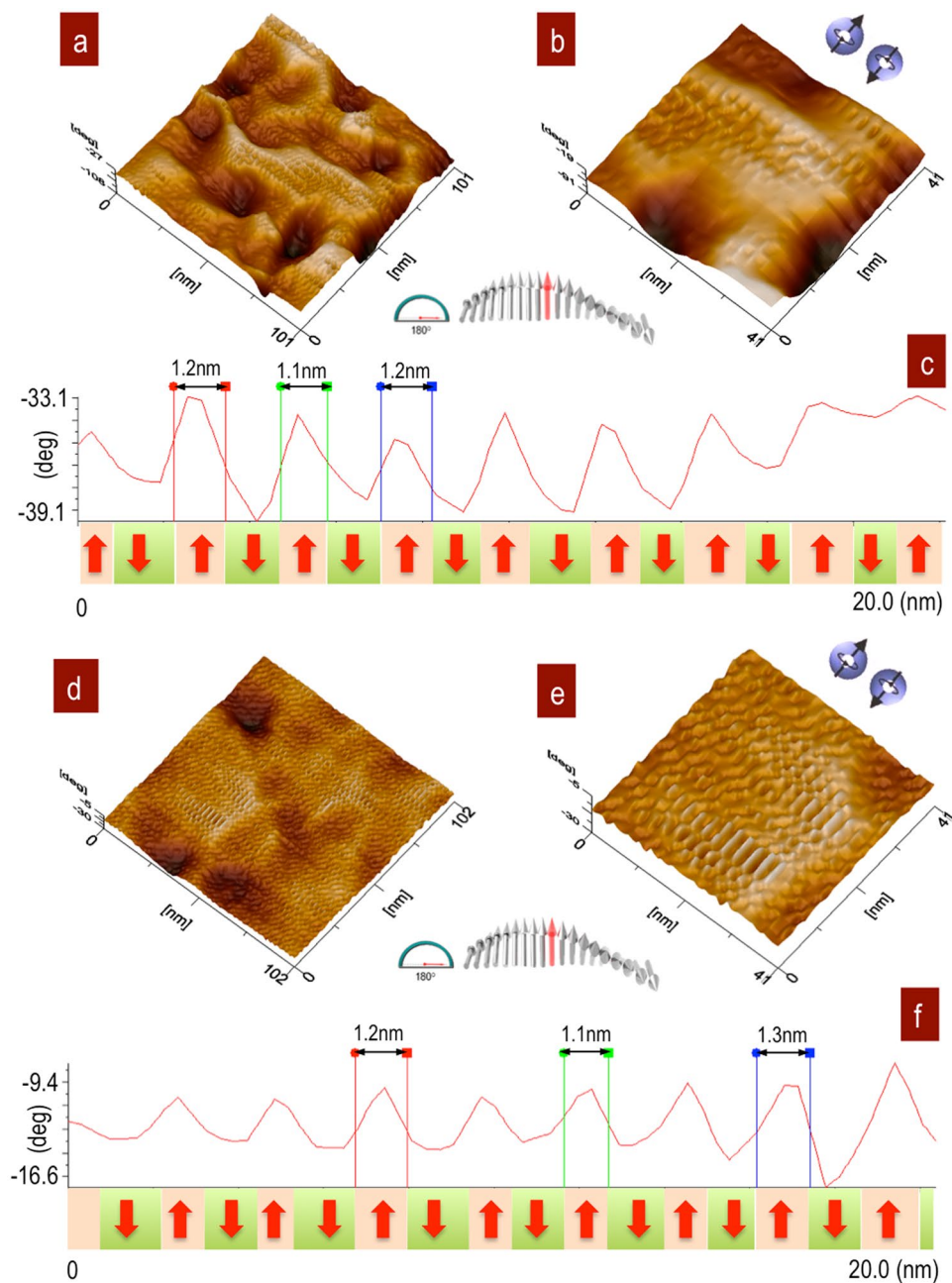


**Figure 6.** Parallel orientation of magnetic domains with uniaxial behaviour. (a)  $\text{Fe}_3\text{O}_4$  SSD immersed in a  $\text{SiO}_2$  matrix after stirring for 4 h show desirable areas with stripes in the same direction, and the profile indicates the orientation of SSD,  $90^\circ$ ; (b) after stirring for 12 h, the sample shows oriented magnetic domains and assembly by neighbouring interactions; profiles show the sum of all local SSD.

particles were washed with ethanol and precipitated with the help of a magnet. They were dried at room temperature, and the powder was characterized.

The analysis of the material allowed determination of the optimal reaction time conditions to reduce the agglomeration in the citrate suspension. Additionally, these samples were processed by the Stöber method to embed the magnetite NPs in the matrix of silicon dioxide. This is an easy methodology to reduce agglomeration and to improve the  $\text{Fe}_3\text{O}_4$  NPs dispersal in the  $\text{SiO}_2$  matrix and the magnetic properties of the magnetite under different stirring conditions.

To determine the properties of the nanostructures, different characterization techniques were used: RIGAKU Smart Lab X-ray diffractometer, XRD, was used in the Bragg-Brentano configuration with 0.02 steps in the range from  $25$  to  $70^\circ$ ,  $2\theta$  with a copper source of  $1.5424 \text{ \AA}$  and wavelength to define  $\text{Fe}_3\text{O}_4/\text{SiO}_2$  structures. PowderCell Software was used to analyse experimental diffractograms from XRD<sup>53,54</sup>. Their dispersion and particle sizes were observed by JEOL-JEM 2010 transmission electron microscope, TEM, with a  $\text{LaB}_6$  filament at an acceleration voltage of 200 kV. The functional groups of silicon and magnetite were examined with an FT-IR



spectrophotometer, NICOLET 6700. The magnetic response was determined using a MPMS3 Magnetometer SQUID of Quantum Design with a sensitivity of  $5 \times 10^{-8}$  emu.

Magnetic force microscopy (MFM) was performed with a scanning probe microscope (SPM) JEOL JSPM 5200 multimodes. The samples were dispersed in carbon adhesive tape over the holder. An ultra-sharp silicon cantilever NSC14/Co-Cr/15 micro-mesh was exposed to a strong neodymium magnet. The voltage and lift conditions were defined according to the magnetic surface interactions of the sample with the tip lift output [0.030–0.1 V].

## References

- Li, Z., Wei, L., Gao, M. Y. & Lei, H. One-pot reaction to synthesize biocompatible magnetite nanoparticles. *Adv. Mater.* **17**, 1001–1005 (2005).
- Marciello, M. *et al.* Large scale production of biocompatible magnetite nanocrystals with high saturation magnetization values through green aqueous synthesis. *J. Mater. Chem. B*, **1**, 5995–6004 (2013).
- Hachani, R. *et al.* Assessing cell-nanoparticle interactions by high content imaging of biocompatible iron oxide nanoparticles as potential contrast agents for magnetic resonance imaging. *Scientific Reports*, **7**, 7850 (2017).
- Ito, A. *et al.* Magnetite nanoparticle-loaded anti-HER2 immunoliposomes for combination of antibody therapy with hyperthermia. *Cancer Lett.* **212**, 167–175 (2004).
- Dobson, J. Remote control of cellular behaviour with magnetic nanoparticles. *Nature Nanotechnology*, **3**, 139–143 (2008).
- McBain, S. C., Yiu, H. H. P. & Dobson, J. Magnetic nanoparticles for gene and drug delivery. **3**, 169–180 (2008).
- Kleinauskas, A. *et al.* Superparamagnetic magnetite nanoparticles for cancer theranostics. *Rev. Nanosci. Nanotechnol.* **1**, 271–283 (2012).
- Lu, Y. C. *et al.* Cellular uptake of magnetite nanoparticles enhanced by NdFeB magnets in staggered arrangement. **427**, 71–80 (2017).
- Noh, S. H. *et al.* Recent advances of magneto-thermal capabilities of nanoparticles: From design principles to biomedical applications. *Nano Today*, **13**, 61–76 (2017).
- Shin, T. H. & Cheon, J. Synergism of nanomaterials with physical stimuli for biology and medicine. *Acc. Chem. Res.* **50**, 567–572 (2017).
- Hou, L., Zhang, H., Wang, L. & Chen, L. Ultrasound-enhanced magnetite catalytic ozonation of tetracycline in water. *Chem. Eng. J.* **229**, 577–584 (2013).
- Legutko, P., Kaspera, W., Stelmachowski, P., Sojka, Z. & Kotarba, A. Boosting the catalytic activity of magnetite in soot oxidation by surface alkali promotion. *Catal. Commun.* **56**, 139–142 (2014).
- Shaghholani, H., Ghoreishi, S. M. & Mousazadeh, M. Improvement of interaction between PVA and chitosan via magnetite nanoparticles for drug delivery application. *Int. J. Biol. Macromol.* **78**, 130–136 (2015).
- Tan, J., Chen, J., Liu, K. & Huang, X. Synthesis of porous  $\alpha$ -Fe<sub>2</sub>O<sub>3</sub> microrods via *in situ* decomposition of FeC<sub>2</sub>O<sub>4</sub> precursor for ultra-fast responding and recovering ethanol gas sensor. *Sens. Actuator B-Chem.* **230**, 46–53 (2016).
- Xu, M., Li, Q. & Fan, H. Monodisperse nanostructured Fe<sub>3</sub>O<sub>4</sub>/ZnO microrods using for waste water treatment. *Adv. Powder Technol.* **25**, 1715–1720 (2014).
- Chandra, S., Mehta, S., Nigam, S. & Bahadur, D. Dendritic magnetite nanocarriers for drug delivery applications. *New J. Chem.* **34**, 648–655 (2010).
- Guo, S., Li, D., Zhang, L., Li, J. & Wang, E. Monodisperse mesoporous superparamagnetic single-crystal magnetite nanoparticles for drug delivery. *Biomaterials* **30**, 1881–1889 (2009).
- Yan, W., Fan, H. & Yang, C. Ultra-fast synthesis and enhanced photocatalytic properties of alpha-Fe<sub>2</sub>O<sub>3</sub>/ZnO core-shell structure. *Mater. Lett.* **65**, 1595–1597 (2011).
- Mornet, S. *et al.* Magnetic nanoparticle design for medical applications. *Prog. Solid State Chem.* **34**, 237–247 (2006).
- Chikazumi, S. *et al.* Physics of magnetic fluids. *J. Magn. Magn. Mater.* **65**, 245–251 (1987).
- Hyeon, T. Chemical synthesis of magnetic nanoparticles. *Chem. Commun.* **8**, 927–934 (2003).
- Ren, X. *et al.* Magnetic force driven noncontact electromagnetic-triboelectric hybrid nanogenerator for scavenging biomechanical energy. *Nano Energy*, **35**, 233–241 (2017).
- Simeonidis, K. *et al.* *In-situ* particles reorientation during magnetic hyperthermia application: Shape matters twice. *Scientific Reports*, **6**, 38382 (2016).
- Yu, X., Cheng, G. & Zheng, S. Y. Synthesis of self-assembled multifunctional nanocomposite catalysts with highly stabilized reactivity and magnetic recyclability. *Scientific Reports*, **6**, 25459 (2016).
- Majetich, S. A. & Jin, Y. Magnetization directions of individual nanoparticles. *Science*, **284**, 470–473 (1999).
- Coe, J. M. D. Magnetostatics in *Magnetism and magnetic materials* 24–50 (Cambridge University Press, 2010).
- Blaney, L. Magnetite (Fe<sub>3</sub>O<sub>4</sub>): properties, synthesis, and applications. Preprint at <http://preserve.lehigh.edu/cas-lehighreview-vol-15/5> (2007).
- Unsoy, G. *et al.* Magnetite: from synthesis to applications. *Curr. Top. Med. Chem.* **15**, 1622–1640 (2015).
- Andrade, A. L., Fabris, J. D., Domingues, R. Z. & Pereira, M. C. Current status of magnetite-based core@shell structures for diagnosis and therapy in oncology short running title: biomedical applications of magnetite@shell structures. *Curr. Pharm. Des.* **21**, 5417–5433 (2015).
- Reichel, V. *et al.* Crystalline superstructured stable single domain magnetite nanoparticles. *Scientific Reports*, **7**, 45484 (2017).
- Darwish, M. S. A., Machunsky, S., Peuker, U., Kunz, U. & Turek, T. Magnetite core-shell nano-composites with chlorine functionality: preparation by miniemulsion polymerization and characterization. *J. Polym. Res.* **18**, 79–88 (2011).
- Rudakovskaya, P. G. *et al.* Synthesis of magnetite-gold nanoparticles with core-shell structure. *Moscow Univ. Chem. Bull.* **70**, 149–156 (2015).
- Hwang, B. *et al.* Preparation of magnetite core-titania shell and hollow titania nanoparticles via layer-by-layer (LbL) assembly method. *Macromol. Res.* **22**, 223–226 (2014).
- Uribe-Madrid, S. I. *et al.* Fabrication of Fe<sub>3</sub>O<sub>4</sub>@mSiO<sub>2</sub> core-shell composite nanoparticles for drug delivery applications. *Nanoscale Res. Lett.* **10**, 217, <https://doi.org/10.1186/s11671-015-0920-5> (2015).
- Sonmez, M. *et al.* Synthesis and applications of Fe<sub>3</sub>O<sub>4</sub>/SiO<sub>2</sub> core-shell materials. *Curr. Pharm. Des.* **21**, 5324–5335 (2015).
- Laurent, S. *et al.* Magnetic iron oxide nanoparticles: synthesis, stabilization, vectorization, physicochemical characterizations, and biological applications. *Chem. Rev.* **108**, 2064–2110 (2008).
- Craik, D. J. & Tebble, R. S. Magnetic domains. *Rep. Prog. Phys.* **24**, 116–166 (1961).
- Hiergeist, R. *et al.* Application of magnetite ferrofluids for hyperthermia. *J. Magn. Magn. Mater.* **201**, 420–422 (1999).
- Stephen, Z. R., Kievit, F. M. & Zhang, M. Magnetite nanoparticles for medical MR imaging. *Materials Today* **14**, 330–338 (2011).
- Yang, L. *et al.* Facile synthesis and paramagnetic properties of Fe<sub>3</sub>O<sub>4</sub>@SiO<sub>2</sub> core-shell nanoparticles. *Superlattices Microstruct.* **76**, 205–212 (2014).
- Larumbe, S., Gómez-Polo, C., Pérez-Landazábal, J. I. & Pastor, J. M. Effect of a SiO<sub>2</sub> coating on the magnetic properties of Fe<sub>3</sub>O<sub>4</sub> nanoparticles. *J. Phys. Condens. Matter.* **24**, 266007–266012 (2012).
- Subagyo, A. & Sueoka, K. Correlation between Surface Structure and Charge Ordering in Magnetite(001) Studied by Scanning Tunneling Microscopy and Spectroscopy. *J. Phys. Conf. Series.* **61**, 1102–1106 (2007).

43. Taylor, A. & Sinclair, H. On the determination of lattice parameters by the Debye-Scherrer method. *Proc Phys Soc.* **57**, 126–135 (1945).
44. Frandsen, C. *et al.* Oriented attachment and exchange coupling of alpha-Fe<sub>2</sub>O<sub>3</sub> nanoparticles. *Phys. Rev. B.* **72**, 214406 (2005).
45. Reufer, M. *et al.* Magnetic properties of silica coated spindle-type hematite particles. *J. Phys.-Condes. Matter.* **23**, 065102 (2011).
46. Hunt, C. P., Moskowitz, B. M. & Banerje, S. K. Magnetic Properties of rocks and minerals, in rock physics & phase relations: a handbook of physical constants (ed T. J. Ahrens) 189–204 (American Geophysical Union, Washington, D. C. 1995).
47. Cullity, B. D. *Introduction to Magnetic Materials* 1st edn (Addison-Wesley, 1972).
48. Jun, Y. W., Seo, J. W. & Cheon, J. Nanoscaling laws of magnetic nanoparticles and their applicabilities in biomedical sciences. *Acc. Chem. Res.* **41**, 179–89 (2008).
49. Goya, G. F., Berquó, T. S., Fonseca, F. C. & Morales, M. P. Static and dynamic magnetic properties of spherical magnetite nanoparticles. *J. Appl. Phys.* **94**, 3520–3528 (2003).
50. Santoyo-Salazar, J. *et al.* Magnetic iron oxide nanoparticles in 10–40 nm range: composition in terms of magnetite/maghemite ratio and effect on the magnetic properties. *Chem. Mater.* **23**, 1379–1386 (2011).
51. Ramirez-Núñez, A. L. *et al.* *In vitro* magnetic hyperthermia using polyphenol-coated Fe<sub>3</sub>O<sub>4</sub>@ $\gamma$ -Fe<sub>2</sub>O<sub>3</sub> nanoparticles from *Cinnamomum verum* and *Vanilla planifolia*: the concert of green synthesis and therapeutic possibilities. *Nanotechnology.* **29**, 074001 (2018).
52. Serrate, D. *et al.* Imaging and manipulating the spin direction of individual atoms. *Nature Nanotechnology.* **5**, 350–353 (2010).
53. Dave, S. R. & Gao, X. Monodisperse magnetic nanoparticles for biodetection, imaging, and drug delivery: a versatile and evolving technology. *Wiley Interdiscip. Rev. Nanomed. Nanobiotechnol.* **1**, 583–609 (2009).
54. Nolze, G. & Kraus, W. PowderCell 2.0 for Windows. *Powder Diff.* **13**(4), 256–259 (1998).

## Acknowledgements

This work was partially supported by the Consejo Nacional de Ciencia y Tecnología (CONACyT). Special thanks to Conacyt, PhD Fellow for J.A.F.G. The authors are grateful to Marcela Guerrero from CINVESTAV-IPN for XRD support, and LANE, CINVESTAV-IPN by the facilities to use the AFM-MFM. Also to Norma Angélica García Vargas Master student of UPIITA-IPN and Marlene González Montiel for the magnetic characterization. from CICATA-IPN Legaria.

## Author Contributions

J.A.F.G. contributed to the synthesis and characterization of Fe<sub>3</sub>O<sub>4</sub> nanoparticles embedded in a SiO<sub>2</sub> matrix, analysed the results and wrote part of the manuscript. A.I.D.C. wrote part of the manuscript. A.G.C. performed the TEM analysis. J.S.S. and MFM-AFM analysed results and wrote part of the manuscript.

## Additional Information

**Supplementary information** accompanies this paper at <https://doi.org/10.1038/s41598-018-23460-w>.

**Competing Interests:** The authors declare no competing interests.

**Publisher's note:** Springer Nature remains neutral with regard to jurisdictional claims in published maps and institutional affiliations.



**Open Access** This article is licensed under a Creative Commons Attribution 4.0 International License, which permits use, sharing, adaptation, distribution and reproduction in any medium or format, as long as you give appropriate credit to the original author(s) and the source, provide a link to the Creative Commons license, and indicate if changes were made. The images or other third party material in this article are included in the article's Creative Commons license, unless indicated otherwise in a credit line to the material. If material is not included in the article's Creative Commons license and your intended use is not permitted by statutory regulation or exceeds the permitted use, you will need to obtain permission directly from the copyright holder. To view a copy of this license, visit <http://creativecommons.org/licenses/by/4.0/>.

© The Author(s) 2018